OpenFOAM® Journal

Volume 6 [Full Papers], Pages 51–59
ISSN: 2753-8168

Implementation of the Elastic to Softening Transition and Rupture Analysis Model in OpenFOAM®

Eduardo Vieira*, Ramon Martins, Marcio Martins, Humberto Belich, and Dario Canossi

Multiphysics Modeling Laboratories (MM Labs), PPGEM, Federal University of Espírito Santo, 514, Av. Fernando Ferrari, Vitória 29.075-910, Brazil
Email address: eduardo.m.vieira@edu.ufes.br

DOI: https://doi.org/10.51560/ofj.v6.165
Results with version(s): OpenFOAM® v7.0 and v9.0 with RheoTool® v6.0x
Repository: https://github.com/EduardoMVieira/ESTRAmodel

Abstract. The accurate modelling of viscoelastic fluids is crucial for various engineering and scientific applications, particularly in polymer processing, biological flows, and complex fluid dynamics. In this study, we implemented a new computational approach for modelling viscoelastic fluids within the OpenFOAM framework. The proposed model incorporates an improved constitutive model that captures both the elastic and dissipative properties of polymeric fluids, ensuring better accuracy in numerical simulations. The results show that ESTRA predicts polymer degradation in the interface between the principal flow and the recirculations.

1. Introduction

The study of viscoelastic fluids is pivotal due to their ubiquitous presence in industrial [1–3] and biological [4–6] systems, such as polymer processing, enhanced oil recovery [7], and blood flow in arteries [8]. These fluids exhibit unique mechanical properties, combining elasticity and viscosity [9], which result in complex flow behaviour under varying stress conditions.

Viscoelastic fluids are highly advantageous for mixing applications, as at low Reynolds numbers, once a threshold criterion is surpassed, elastic phenomena become dominant, leading to the emergence of elastic turbulence. This turbulent state enhances mixing efficiency due to the inherently diffusive nature of turbulent flows [10].

One of the critical challenges in studying viscoelastic fluids is polymer degradation, a process where mechanical forces cause the rupture of polymer chains. This degradation significantly alters the fluid's rheological properties, impacting its performance in applications. For instance, in polymer extrusion or inkjet printing, degradation leads to inconsistent product quality, while in biological systems, it may influence critical functions such as nutrient transport or clot formation.

Although the existing viscoelastic models provide insights into viscoelastic behavior, all models fail in capturing the intricate mechanisms of polymer rupture and its effect on fluid dynamics. One of the well-constructed models is the Oldroyd-B [11] model, which has the following constitutive equation [12]:

$$\lambda \overset{\nabla}{\mathbf{A}} = -\mathbf{A} + \mathbf{I} \,, \tag{1}$$

in which λ is the relaxation time, $\mathbf{A}$ is the conformation tensor, $\mathbf{I}$ is the identity tensor, and $\overset{\nabla}{(\,)}$ is the upper-convected time derivative [13, 14].

Another classic viscoelastic fluid model is the Finitely Extensible Nonlinear Elastic model with Peterlin's closure (FENE-P) [15]. It imposes a restriction on the polymer stretching; however, it leads to an asymptotic behavior near the extension limit. The FENE-P constitutive equation is

* Corresponding author

Received: 30 April 2025, Accepted: 2 January 2026, Published: 9 March 2026

©2026 The Authors. This work is an open access article under the CC BY-SA 4.0 license

$$\lambda \overset{\nabla}{\mathbf{A}} = -\left(\frac{L^2}{L^2 - \mathrm{tr}(\mathbf{A})}\right)\mathbf{A} + \left(\frac{L^2}{L^2 - 3}\right)\mathbf{I}\,. \tag{2}$$

Herein, L^2 is related to a dimensionless length parameter expressing the limit of extension of the polymer chain, and tr( ) is the trace operator. Also, observe that the trace of the conformation tensor (tr($\mathbf{A}$)) gives an idea of the stretching of the polymer.

Both models fail to predict polymer degradation. Oldroyd-B has a nonphysical stretching behavior that extends infinitely [16–18], while FENE-P has the opposite behavior, a stretching limit that causes an infinite stress [18, 19].

In a previous work [20], we propose a modification in the FENE spring equation, by removing its singularity and accounting for a softening regime. We then applied the spring force equation in the Fokker-Planck equation in another article (more information in [21]) and obtained a continuous version of the fluid model. The Elastic to Softening Transition and Rupture Analysis (ESTRA) model constitutive equation is defined as

$$\lambda \overset{\nabla}{\mathbf{A}} = -\frac{L^2 + \gamma \mathrm{tr}(\mathbf{A})}{L^2}\mathbf{A} + \frac{L^2}{L^2 - 3}\mathbf{I}\,, \tag{3}$$

where γ is the transition from elastic to softening regime function, and we implemented it by a function of the polymeric stress ($\boldsymbol{\tau}_p$),

$$\gamma = \frac{\tau_0 - |\mathrm{tr}(\boldsymbol{\tau}_p)|}{\tau_0}\,, \tag{4}$$

in which, τ_0 is the polymeric stress limit of the elastic regime. Observe that in the absence of extensional polymeric stress ($\mathrm{tr}(\boldsymbol{\tau}_p) = 0$), $\gamma = 1$, if the trace of the polymeric stress is equal to τ_0, $\gamma = 0$ and the polymer chain transitions from the elastic to the softening regime. Furthermore, observe that increasing even more the extensional stress acting in the polymer, $\gamma < 0$. In a nutshell, if $0 \leq \gamma \leq 1$, the polymer chain is in the elastic regime, while if $-\infty < \gamma < 0$, it is in the softening regime.

We emphasise that in our model, L^2 no longer retains its physical interpretation as the limiting stretch of a polymer chain; instead, it serves solely as a dimensionless length parameter.

Polymer degradation occurs where the breaking criterion is satisfied in the spatial domain,

$$\mathrm{tr}(\mathbf{A}) > \frac{L^2}{|\gamma|}\,. \tag{5}$$

Lastly, the L^2 property is advected by a transport equation, as follows:

$$\frac{\partial L^2}{\partial t} + \nabla \cdot (\mathbf{u} L^2) = 0 \tag{6}$$

Building upon our previous work [20, 21], we extend the concept from single spring mechanics to a continuous medium representation, enabling the integration of polymer degradation dynamics into computational fluid dynamics (CFD) simulations using Finite Volume Method (FVM) in OpenFOAM®. The ESTRA model is designed to predict rupture events and their impact on flow, offering a robust tool to advance the understanding of the behavior of viscoelastic fluid.

2. Implementation in OpenFOAM®

We implemented the ESTRA model in RheoTool®, an open-source toolbox based on OpenFOAM® (Open Field Operation And Manipulation), developed to simulate Generalised Newtonian Fluids (GNF) and viscoelastic fluids under pressure-driven and/or electrically-driven flows. It offers a range of features, including support for 2D/3D problems on generic grids, fully parallelised code with MPI (Message Passing Interface) for continuum mechanics, compatibility with moving or static meshes, and a wide array of rheological models. RheoTool® also includes a Brownian dynamics solver to simulate polymer molecules individually.

The viscoelastic models can be solved using the constitutive equation in terms of the conformation tensor or in terms of the polymeric stress. In the case of ESTRA, $\boldsymbol{\tau}_p$ is related to $\mathbf{A}$ through

$$\boldsymbol{\tau}_p = \frac{\eta_p}{\lambda}\left(f\mathbf{A} - a\mathbf{I}\right) \tag{7}$$

and we decided to implement only the formulation in terms of $\mathbf{A}$ because the RheoTool® solver is more stable than operating with $\boldsymbol{\tau}_p$ [22]. Additionally, η_p is the polymeric viscosity.

As exposed in the previous section, ESTRA was based on the FENE-P model. The FENE-P model is implemented in the RheoTool® package using the Eqn. 3, in which the first fraction in the RHS is the f variable and the second fraction is the a variable, as illustrated in Lst. 1.

```
a = L2_/(L2_-3);
varF_ = (1/(1-tr(A_)/L2_));
```

Listing 1. Calculation of FENE-P auxiliary variables, a, and f based on the global value of L^2 and the conformation tensor trace.

For ESTRA, following Lst. 2, we first calculate a given the volumetric value of L^2 (line 200), in sequence, γ is calculated given the $\boldsymbol{\tau}_p$ field and the scalar τ_0 (line 201). Later, f is calculated given the L^2, γ and the conformation tensor ($\mathbf{A}$) fields (line 202).

```
200 volScalarField a(L2_/(L2_ - 3));
201 gamma_ = 1.0 - mag(N1_)/tau0_;
202 varF_ = 1.0 + (gamma_*(tr(A_))/L2_);
```

Listing 2. Calculation of ESTRA auxiliary variables, a, γ, and f based on the local values of L^2, the conformation tensor trace, and the polymeric stress field.

The $\mathbf{A}$ equation (Eqn. 3) is then solved from lines 204 to 216 from Lst. 3.

```
204 // Stress transport equation
205    fvSymmTensorMatrix AEqn
206    (
207        fvm::ddt(A_)
208      + fvm::div(phi(), A_)
209     ==
210        twoSymm(C)
211     -  fvm::Sp(varF_/lambda, A_)
212     +  (a/lambda) * Ist
213    );
214
215 AEqn.relax();
216 AEqn.solve();
```

Listing 3. Conformation tensor transport equation for the ESTRA model.

In the next step, γ and f are recalculated with the new value of $\mathbf{A}$, as shown in Lst. 4.

```
218 gamma_ = 1.0 - mag(N1_)/tau0_;
219 varF_ = 1.0 + (gamma_*(tr(A_))/L2_);
```

Listing 4. Recalculation of γ and f with the new $\mathbf{A}$ value.

In sequence, as seen in Lst. 5, $\boldsymbol{\tau}_p$ is calculated (by Eqn. 7).

```
221 tau_ = (etaP/lambda) * (varF_*A_ - a*Ist);
222
223 tau_.correctBoundaryConditions();
```

Listing 5. Polymeric stress calculation and correction of boundary conditions (if needed).

At this point, following Lst. 6, we perform the breaking test to determine whether any of the cells of the spatial discretisation satisfy the breaking criterion.

Note that this is a local test that compares the trace of the conformation tensor with the dimensionless length parameter and the transition to the softening regime function. If the criterion is satisfied, L increases by 2%, resulting in L^2 increasing by 4.04%.

```
// Breaking test
    if (std::fmod(iteration_, breakingInterval_) == 0)
    {
        forAll(A_, celli)
        {
            if ((tr(A_[celli])) > (L2_[celli]/mag(gamma_[celli])))
            {
                L2_[celli] = (L2_[celli])*1.0404;
            }
        }
    }
```

Listing 6. Local polymer rupture test applied periodically during the simulation, updating the dimensionless length parameter, L^2, where the breaking criterion is satisfied.

The outer **if** condition was included to allow the user to specify the range of iterations during which the rupture test will be performed, aiming to avoid potential numerical issues. To conduct the test at every time step, set the value to one in the `constitutiveProperties` dictionary.

Finally, L^2 is advected by a transport equation, being the respective code provided in Lst. 7.

```
// L2 equation for advection
    fvScalarMatrix L2Eqn
    (
        fvm::ddt(L2_)
     ==
      - fvm::div(phi(), L2_)
    );

    L2Eqn.relax();
    L2Eqn.solve();

    iteration_++;
```

Listing 7. Transport equation used to advect the dimensionless length parameter, L^2, throughout the computational domain.

3. Simulation methodology

In this section, we present the methodology for simulating the ESTRA model in a 2D sudden expansion/contraction scenario to observe the temporal response and polymer degradation.

The geometry comprises a channel with a length and height (h) of 1 meter, which undergoes a sudden expansion to a height (H) of 2 meters over a length of 1 meter. Subsequently, the channel abruptly contracts back to its original height, with the contracted section also extending for 1 meter.

Since the fluid is incompressible,

$$\nabla \cdot \mathbf{u} = 0 \ , \tag{8}$$

being $\mathbf{u}$ the velocity vector.

The momentum conservation equation is

$$\rho \left(\frac{\partial \mathbf{u}}{\partial t} + \mathbf{u} \cdot \nabla \mathbf{u} \right) = -\nabla p + \nabla \cdot \mathbf{T} \ , \tag{9}$$

with ρ the density of the fluid, t the time, p the pressure, and $\mathbf{T}$ the total extra-stress tensor, which is the sum of the solvent and the polymeric stresses:

$$\mathbf{T} = \boldsymbol{\tau}_s + \boldsymbol{\tau}_p \ , \tag{10}$$

in which $\boldsymbol{\tau}_s$ accounts for the Newtonian contribution,

$$\boldsymbol{\tau}_s = \eta_s \dot{\boldsymbol{\gamma}} \ , \tag{11}$$

Herein, η_s is the solvent viscosity, and $\dot{\boldsymbol{\gamma}} = \nabla \mathbf{u} + (\nabla \mathbf{u})^T$ the deformation rate.

We define the Reynolds number (Re), the Weissenberg number (Wi), and the viscosity ratio (β) as

$$\begin{aligned} Re &= \frac{\rho U h}{\eta_s + \eta_p} \\ Wi &= \frac{\lambda U}{h} \\ \beta &= \frac{\eta_s}{\eta_s + \eta_p} \end{aligned} \quad . \tag{12}$$

The velocity boundary conditions are uniform inlet in the $x-$ direction, $\mathbf{u} = (U, 0) = (1, 0)$ m/s, null gradient at the outlet, $\nabla \mathbf{u} = 0$, and no-slip in the walls $\mathbf{u} = 0$ m/s. The pressure has zero gradients in the walls and the inlet, $\nabla p = 0$, and atmospheric pressure in the outlet, $p = 0$ N/m^2. Lastly, $\mathbf{A} = 0$ in the inlet, and zero gradient, $\nabla \mathbf{A} = 0$ in the walls and the outlet.

4. **Results and discussions**

We simulated three different Weissenberg numbers (Wi), 0.1, 0.5, and 1, to demonstrate the role of the elastic force in the velocity field. This implementation was also utilized to solve the cases in our previous work [21]; however, we don't delve too deeply into the coding in this paper.

Figure 1 presents the velocity profiles of the ESTRA model at $Re = 1$, $\beta = 0.01$, and different Weissenberg numbers (Wi) in a viscoelastic flow, with a Newtonian case ($Wi = 0$) included for comparison. The velocity profiles are evaluated along the y-direction at the midsection of the expanded region. Panel (a) illustrates the streamwise velocity component (u_x) normalized by the inlet velocity (U), where the Newtonian case and the lowest Weissenberg number ($Wi = 0.1$) exhibit a nearly Gaussian shape. However, for $Wi = 0.5$, a subtle change in concavity emerges near $|y/H| \approx 0.6$, which becomes more pronounced at $Wi = 1$. At this highest Weissenberg number, the profile even shows a small region of negative velocity close to the walls, suggesting a flow reversal due to recirculation effects. Panel (b) presents the transverse velocity component (u_y), where deviations from the Newtonian case become increasingly evident as Wi increases. Higher Wi results in larger fluctuations in u_y, which highlights the influence of viscoelasticity on flow behavior, modifying velocity distributions and generating non-trivial flow patterns. In panels (c) and (d), we expose the velocity components u_x and u_y, respectively, at $Wi = 1$; in both panels, we compare ESTRA, FENE-P, and Oldroyd-B models.

By comparing the curves in panels (c) and (d) of Fig. 1, it is possible to visualize that the three models have similar behaviours; however, they are not identical. For instance, ESTRA exhibits a higher u_x value in the middle of the channel, while (by mass conservation) ESTRA has a narrower profile, which is evident near $|y/H| = 0.5$. ESTRA also exposes the highest peaks in the u_y profile near $y/H = 0.25$, while it has the lowest peaks near $y/H = 0.5$.

Figure 2 illustrates the velocity fields and streamlines for a Newtonian fluid and an ESTRA model fluid at different Weissenberg numbers (Wi). Panel (a) shows the Newtonian case ($Wi = 0$), where two symmetric recirculation regions appear in the upper and lower corners of the expanded section. As viscoelastic effects increase in panels (b)–(d), the flow structure undergoes notable changes. At $Wi = 0.1$, the overall structure remains similar to the Newtonian case, but slight asymmetries emerge. At $Wi = 0.5$, the upstream recirculation zones shrink and the downstream vortex intensifies, indicating a change in flow behavior due to elastic stresses. In the most elastic case ($Wi = 1$), a striking transformation occurs: the upstream recirculation is almost completely suppressed, while a single large vortex dominates the downstream region. These results highlight the role of viscoelasticity in altering flow separation and recirculation, demonstrating the non-linear interaction between elasticity and inertia in the ESTRA model. Panels (e) and (f) expose the simulation of, respectively, FENE-P and Oldroyd-B models at $Wi = 1$, for comparison with the last case of ESTRA. Although all models have similar patterns, they have a small difference in the expanded section. For instance, observe the pattern in the middle of the channel and the magnitude of the velocity just before the fluid enters the expanded section.

Since Wi accounts for elastic effects, experimentally it can be related to polymer concentration (remaining the same type of polymer solute), thus, it is expected that, as Wi increases, there may be a greater likelihood of polymer degradation.

Figure 3 presents the L^2 field for Wi numbers, illustrating the spatial distribution of the dimensionless length parameter within the flow. At the lowest Weissenberg number ($Wi = 0.1$), shown in panel (a), the L^2 values remain relatively low and concentrated in the sharp corners and near the entrance region. As viscoelastic effects become more pronounced at $Wi = 0.5$ (panel b), more degradation occurs, particularly near the expansion and contraction regions, where abrupt geometric transitions amplify elastic effects.

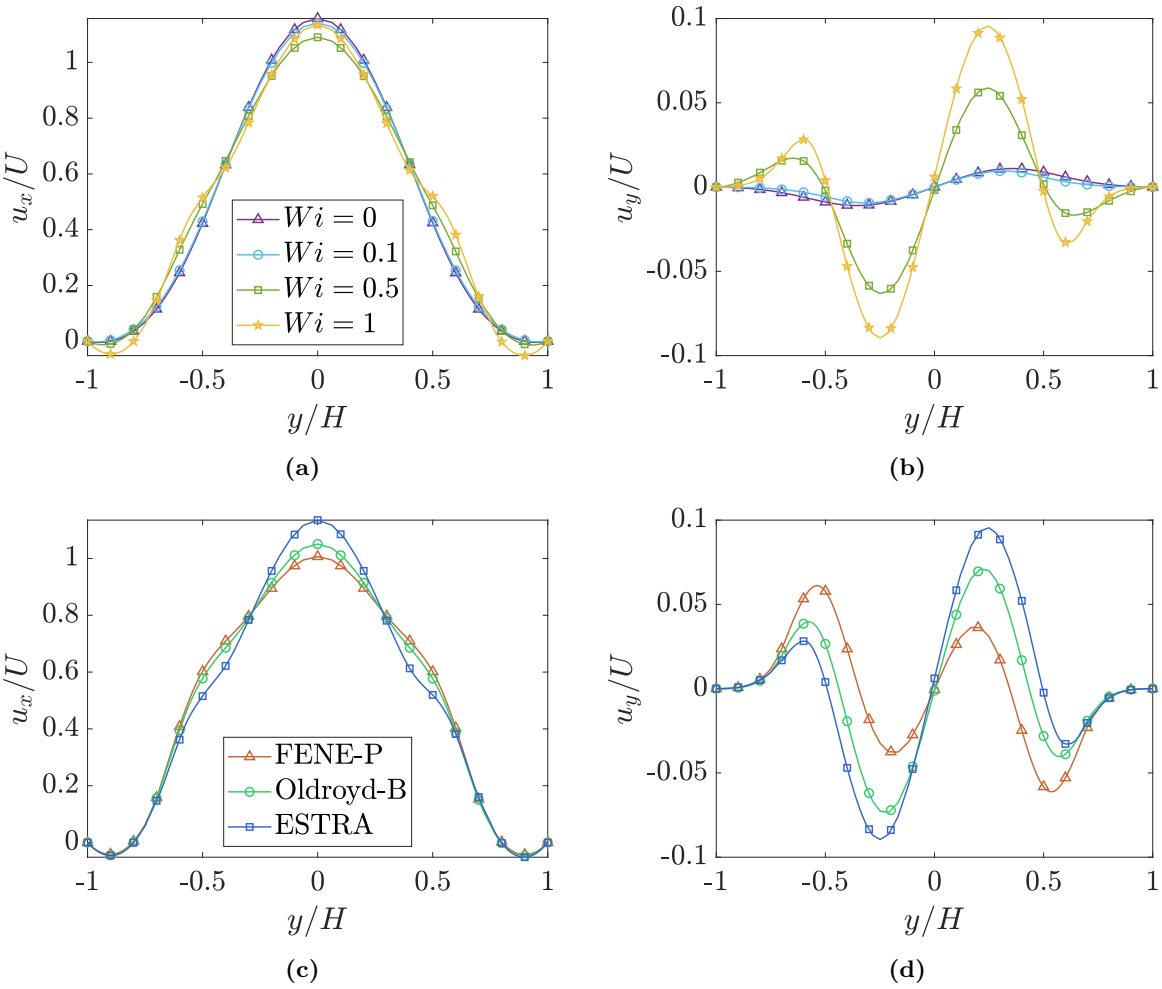

Figure 1. Velocity profiles with three different Weissenberg numbers, 0.1, 0.5, and 1. For comparison, a Newtonian fluid profile is plotted ($Wi = 0$). The line is placed in the $y-$ direction, in the half of the expanded part. Panel (a) shows the u_x profile; it is evident that while a Newtonian fluid and a low Weissenberg number exhibit a Gaussian curve, $Wi = 0.5$ started to show a change of concavity near $|y/H| = 0.6$, which became more prominent at the higher Weissenberg, which also exposed a negative velocity near the walls. Panel (b) shows the u_y velocity profile, which has higher magnitude values as Wi increases. Panel (c) shows the velocity in the $x-$ direction of ESTRA at $Wi = 1$ in comparison with FENE-P and Oldroyd-B, while panel (d) shows the comparison in the $y-$ direction.

At $Wi = 1$ (panel c), the degradation phenomenon intensifies significantly, with noticeable peaks forming near the re-entrant corners of the expansion and contraction zones.

5. Conclusion

We implemented a new viscoelastic fluid model in OpenFOAM® v7.0 and v9.0 using RheoTool® v6.0. We simulated the ESTRA fluid model in a sudden expansion/contraction to observe the elastic contribution within the flow. We also exposed the polymer degradation patterns, which were prominent in the interface between the principal flow and the recirculations in the expanded section.

For comparison purposes, we also simulated Oldroyd-B and FENE-P fluid models within the flow, to observe the patterns. We observe similar patterns between all models, although each one has its differences. ESTRA predicted polymer degradation in the interface between the principal flow and the recirculations.

The model, both in its original formulation and within the log-conformation framework, is publicly accessible on GitHub (see the repository link at the top of this document). This resource facilitates further

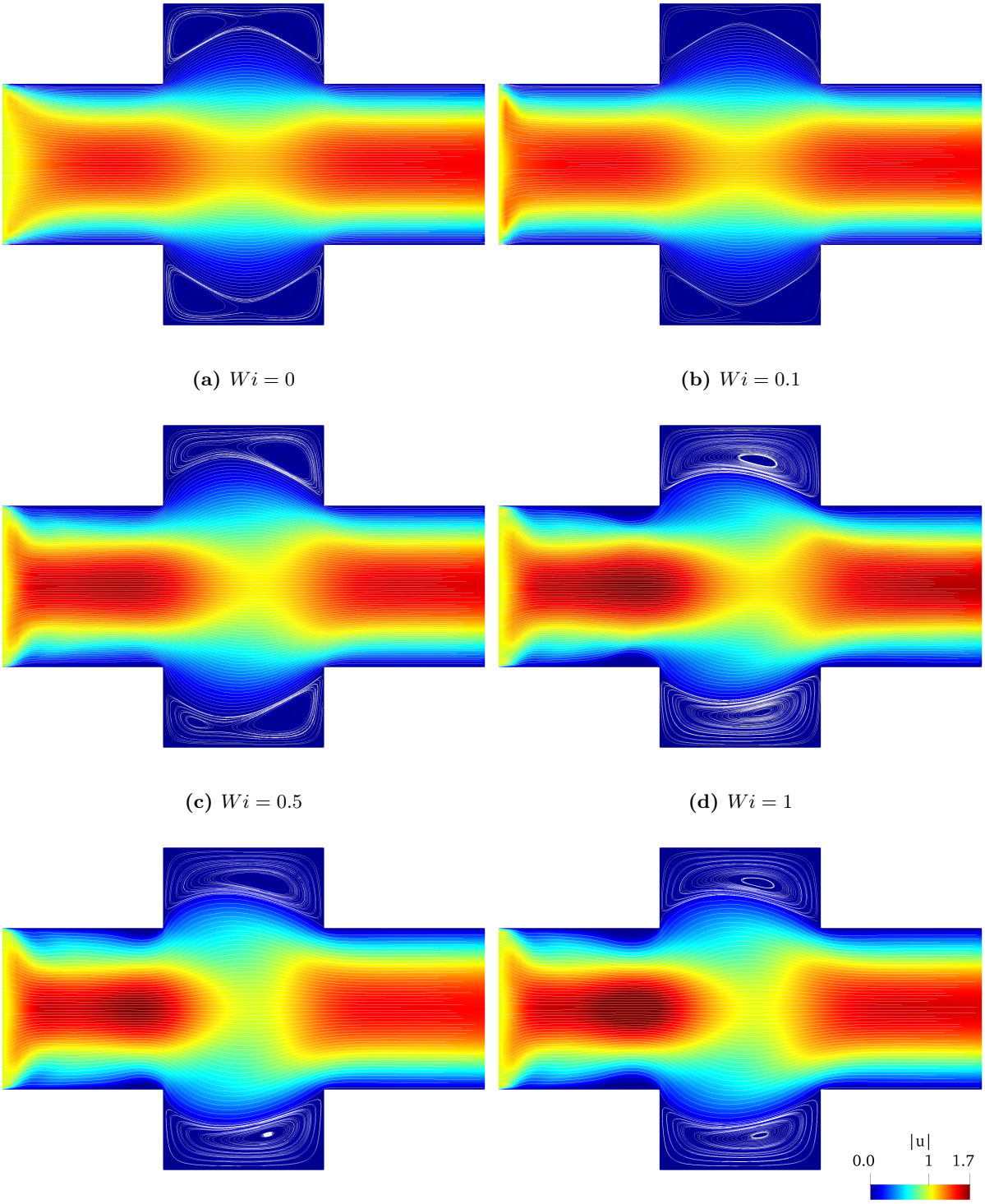

(a) $Wi = 0$ **(b)** $Wi = 0.1$

(c) $Wi = 0.5$ **(d)** $Wi = 1$

(e) $Wi = 1$, FENE-P **(f)** $Wi = 1$, Oldroyd-B

Figure 2. Velocity fields and streamlines for (a) a Newtonian fluid, and an ESTRA model fluid at (b) $Wi = 0.1$, (c) $Wi = 0.5$, and (d) $Wi = 1$. The Newtonian fluid exhibits two recirculations in the upper and lower parts, with symmetric behavior. As the elastic forces gain relevance, the upstream recirculation becomes smaller and the downstream recirculation greater. At $Wi = 1$, there is only one recirculation. Panels (e) and (f) show, respectively, the FENE-P and Oldroyd-B models at $Wi = 1$.

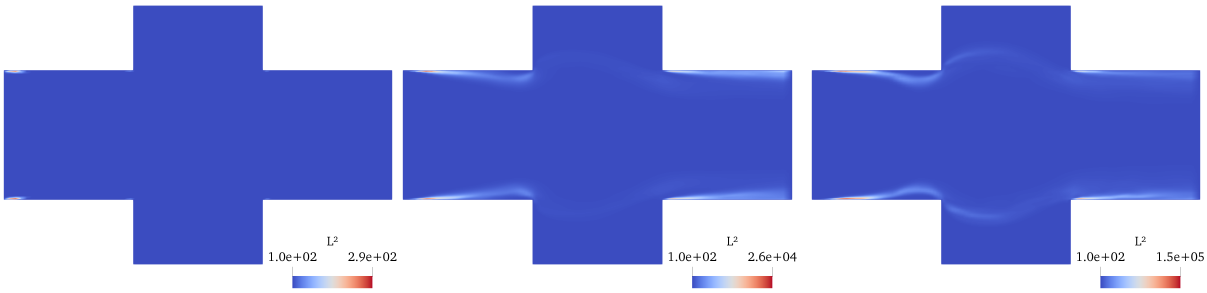

(a) $Wi = 0.1$ **(b)** $Wi = 0.5$ **(c)** $Wi = 1$

Figure 3. Contours of the L^2 field for different Weissenberg numbers. Panel (a) corresponds to $Wi = 0.1$, (b) to $Wi = 0.5$, and (c) to $Wi = 1$. As Wi increases, higher values of L^2 become more localized near the expansion and contraction regions, indicating an intensification of elastic effects and stress concentration in these areas.

advancements in the computational simulation of viscoelastic fluid dynamics, specifically incorporating the phenomenon of polymer degradation.

In the GitHub repository, we also added all the cases used in this article. The ESTRA cases need OpenFOAM® v7.0 or v9.0 with RheoTool® v6.0 solver package. The Newtonian case was tested in OpenFOAM® v9.0, and we prepared the case to be solved by icoFoam or simpleFoam, just change the solver in the control dictionary. For more information about the installation of the ESTRA model, see the readme file.

Acknowledgements

Eduardo Vieira acknowledges the financial support from FAPES for his Ph.D. funding - Grant term 319/2024.

Author Contributions: Writing—original draft preparation, E.V.; writing—review and editing, D.C. and R.M.; investigation, E.V., R.M. and H.B.; software, E.V. and D.C.; methodology, R.M.; formal analysis, H.B.; supervision, M.M. and R.M.; resources, M.M.; project administration, M.M. All authors have read and agreed to the published version of the manuscript.

References

[1] M. M. Denn, "Issues in viscoelastic fluid mechanics," *Annual Review of Fluid Mechanics*, vol. 22, no. 1, pp. 13–32, 1990.
[2] E. C. Coelho, K. C. Barbosa, E. J. Soares, R. N. Siqueira, and J. C. Freitas, "Okra as a drag reducer for high reynolds numbers water flows," *Rheologica Acta*, vol. 55, pp. 983–991, 2016.
[3] I. Pérez-Reyes, R. O. Vargas-Aguilar, S. B. Pérez-Vega, and A. S. Ortiz-Pérez, "Applications of viscoelastic fluids involving hydrodynamic stability and heat transfer," *Polym. Rheol*, vol. 29, 2018.
[4] R. Denton, W. Forsman, S. Hwang, M. Litt, and C. Miller, "Viscoelasticity of mucus: Its role in ciliary transport of pulmonary secretions," *American Review of Respiratory Disease*, vol. 98, no. 3, pp. 380–391, 1968.
[5] E. S. Chase and R. Shafer, "Viscoelastic behavior of mammalian dna," *Biophysical Journal*, vol. 28, no. 1, pp. 93–105, 1979.
[6] J. R. Stokes and G. A. Davies, "Viscoelasticity of human whole saliva collected after acid and mechanical stimulation," *Biorheology*, vol. 44, no. 3, pp. 141–160, 2007.
[7] V. C. Ibezim, R. J. Poole, and D. J. Dennis, "Viscoelastic fluid flow in microporous media," *Journal of Non-Newtonian Fluid Mechanics*, vol. 296, p. 104638, 2021.
[8] G. B. Thurston, "Rheological parameters for the viscosity viscoelasticity and thixotropy of blood," *Biorheology*, vol. 16, no. 3, pp. 149–162, 1979.
[9] D. O. Canossi, G. Mompean, and S. Berti, "Elastic turbulence in two-dimensional cross-slot viscoelastic flows," *Europhysics Letters*, vol. 129, no. 2, p. 24002, 2020.
[10] A. Groisman and V. Steinberg, "Elastic turbulence in a polymer solution flow," *Nature*, vol. 405, no. 6782, pp. 53–55, 2000.
[11] J. G. Oldroyd, "On the formulation of rheological equations of state," *Proceedings of the Royal Society of London. Series A. Mathematical and Physical Sciences*, vol. 200, no. 1063, pp. 523–541, 1950.
[12] C. Viezel, M. F. Tomé, F. Pinho, and S. McKee, "An oldroyd-b solver for vanishingly small values of the viscosity ratio: Application to unsteady free surface flows," *Journal of Non-Newtonian Fluid Mechanics*, vol. 285, p. 104338, 2020.
[13] T.-W. Pan, J. Hao, and R. Glowinski, "On the simulation of a time-dependent cavity flow of an oldroyd-b fluid," *International Journal for Numerical Methods in Fluids*, vol. 60, no. 7, pp. 791–808, 2009.

[14] R. Fattal and R. Kupferman, "Constitutive laws for the matrix-logarithm of the conformation tensor," *Journal of Non-Newtonian Fluid Mechanics*, vol. 123, no. 2-3, pp. 281–285, 2004.
[15] A. Peterlin, "Hydrodynamics of macromolecules in a velocity field with longitudinal gradient," *Journal of Polymer Science Part B: Polymer Letters*, vol. 4, no. 4, pp. 287–291, 1966.
[16] J. Eggers, M. A. Herrada, and J. Snoeijer, "Self-similar breakup of polymeric threads as described by the oldroyd-b model," *Journal of fluid mechanics*, vol. 887, p. A19, 2020.
[17] J. Hinch and O. Harlen, "Oldroyd b, and not a?" *Journal of Non-Newtonian Fluid Mechanics*, vol. 298, p. 104668, 2021.
[18] H. A. C. Sánchez, M. R. Jovanović, S. Kumar, A. Morozov, V. Shankar, G. Subramanian, and H. J. Wilson, "Understanding viscoelastic flow instabilities: Oldroyd-b and beyond," *Journal of Non-Newtonian Fluid Mechanics*, vol. 302, p. 104742, 2022.
[19] V. Tirtaatmadja and T. Sridhar, "Comparison of constitutive equations for polymer solutions in uniaxial extension," *Journal of Rheology*, vol. 39, no. 6, pp. 1133–1160, 1995.
[20] H. Belich, M. Ferreira Martins, R. Silva Martins, L. Silva Amorim, and E. Marques Vieira, "From the fene model to polymer rupture," *Brazilian Journal of Physics*, vol. 55, no. 1, p. 15, 2025.
[21] E. Marques Vieira, R. Silva Martins, M. Ferreira Martins, H. Belich, and L. Silva Amorim, "Modeling polymer rupture: The elastic to softening transition and rupture analysis model," *Physics of Fluids*, vol. 37, no. 3, 2025.
[22] F. Pimenta and M. Alves, "rheotool," https://github.com/fppimenta/rheoTool, 2016.